small methods
www.small-methods.com

Enhancing Performance of GaN/Ga_2O_3 P-N Junction Uvc Photodetectors via Interdigitated Structure

*Ziling Cai, Xiyao He, Kaikai Wang, Xin Hou, Yang Mei, Leiying Ying, Baoping Zhang, and Hao Long**

Ga_2O_3-based Ultraviolet-C photodetector (UVCPD) is considered the most promising UVCPD at present and is divided into Metal-Semiconductor-Metal (MSM) and PN junction types. Compared with MSM-PDs, PN-PDs exhibit superior transient performance due to the built-in electric field. However, current Ga_2O_3-based PN-PDs lack consideration for carrier collection and electric field distribution. In this study, PN-PDs with an interdigital n-Ga_2O_3 layer and finger electrodes are fabricated on p-GaN/n-Ga_2O_3 epilayers. Ultrafast response times of 31 µs (1/e decay) and 2.76 µs (fast component) are realized, which outperforms all Ga_2O_3 UVC-PDs up to now. Under 0 V self-powered, the responsivity (0.25 A W^{-1}) of interdigital PD is enhanced by the interdigital electrode structure due to increasing carriers' collection length. Under bias, the performances of interdigital PD with 41.7 A W^{-1} responsivity and 8243 selection ratios are significantly elevated by enhancing the built-in electric field in the Ga_2O_3 region, which is 34.76 and 39.4 times those of traditional PDs, respectively. The intrinsic enhancing mechanism of interdigital structure is also investigated by interdigital PDs with various electrode spacings and perimeters. In summary, this paper not only reports a highly performed interdigitated structure p-GaN/n-Ga_2O_3 UVCPDs, but also provides guidelines for structure design in Ga_2O_3-based PN-PDs.

1. Introduction

Solar blind Ultraviolet-C (200–280 nm) photodetectors (UVC PDs) are widely used in flame sensing, pollution monitoring, invisible optical communication, ozone monitoring, UV emitter calibration and missile warning.[1–3] Traditional UVC PDs are typically based on silicon or silicon carbide. However, their narrow bandgaps of 1.14 and 3.2 eV require additional filters to absorb infrared, visible and UVA-UVB photons, which increases the cost and instability.[4] To address these issues, previous studies have suggested wide-bandgap materials,[5] such as AlGaN,[6] AlN,[7] diamond,[8] ZnMgO,[9] and Ga_2O_3.[10–12] However, AlGaN, AlN, diamond and ZnMgO suffer from poor epitaxial quality,[13,14] over bandgaps and complex alloying processes.[15,16] β-Ga_2O_3 with a 4.85 eV (255 nm) bandgap has emerged as a promising material for UVC PD recently,[17–19] due to its suitable bandgap, high absorption, and mature bulk fabrication. β-Ga_2O_3-based UVC PDs can be classified into PN hetero-junctions (due to a lack of p-Ga_2O_3) and MSM thin film structures.[20–25] Among them, PN junction PDs with typical n-Ga_2O_3 and other p-type semiconductors exhibit outstanding advantages, such as low dark current, fast response speed and high responsivity due to the PN built-in electric field. The photogenerated electron-hole pairs can be automatically separated by the built-in electric field,[26–30] rendering self-powered photovoltaic sensing with promising applications in communication and space detection.[31–33] Consequently, β-Ga_2O_3-based PN UVC PDs have been widely studied in recent years. For instance, in 2018, Guo et al. combined p-type GaN with n-type Sn-doped β-Ga_2O_3 to fabricate a self-powered ultraviolet photodetector.[34] Under zero bias and 254 nm illumination, the responsivity reached 3.05 A W^{-1}. In 2019, Li et al. reported the achievement of an n-Ga_2O_3/p-CuSCN core-shell microwire heterojunction photodetector with a suppression ratio ($R_{254\ nm}/R_{365\ nm}$) of 1.15×10^4, responsivity of 13.3 mA W^{-1}, and rise/decay times of 62 ms/35 ms at 5 V bias.[35] Similarly, in 2019, Yu et al. utilized pulsed laser deposition to grow β-Ga_2O_3 films on 4H-SiC templates, resulting in the fabrication of a photodetector with a responsivity of 10.35 mA W^{-1} and rise/decay times of 1 ms/19 ms.[36] In 2023, Chen et al. reported achieving 7 ms/19 ms rise/decay times by inserting an i-Ga_2O_3 layer into a self-powered p-GaN/i-Ga_2O_3 /n-Ga_2O_3 (pin) photodetector.[37] However, all the above β-Ga_2O_3-based PN UVC PDs employed pad electrode structures with large electrode spacing and a low electrode perimeter/area ratio, resulting in inferior carrier collection efficiency at 0 V and a weak electric field at negative bias.[38] Interdigital cross-finger structures, whose positive and negative electrodes are paved periodically with small spacing (<100 µm) have been widely used in piezoelectric filters (Surface/Bulk Acoustic Wave Filter, etc.) and MSM-PDs.[39,40] Due to its narrow electrode spacing, the electric fields could be enhanced

Z. Cai, X. He, K. Wang, X. Hou, Y. Mei, L. Ying, B. Zhang, H. Long
School of Electronic Science and Engineering (National Model Microelectronics College)
Xiamen University
Xiamen, Fujian 361005, China
E-mail: longhao@xmu.edu.cn

The ORCID identification number(s) for the author(s) of this article can be found under https://doi.org/10.1002/smtd.202301148

DOI: 10.1002/smtd.202301148

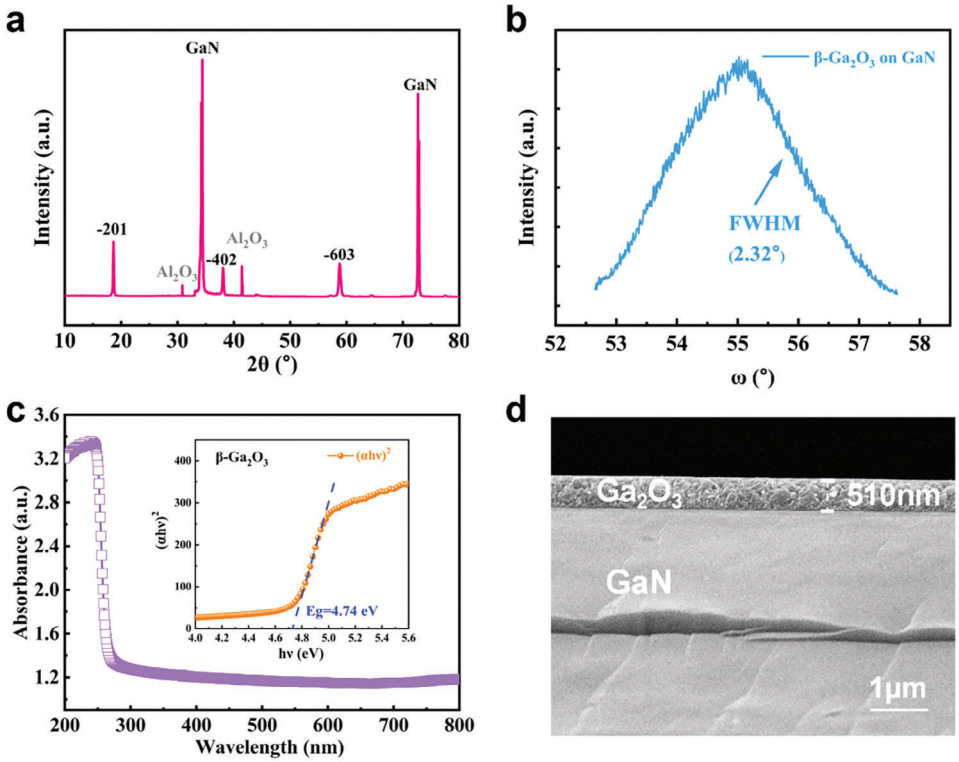

Figure 1. a) XRD phase analysis of the GaN/β-Ga_2O_3 epilayer. b) Rocking curve of the ($\bar{2}$01) plane of β-Ga_2O_3 on p-GaN. c) Absorption spectrum of β-Ga_2O_3 film with inset Tauc plot. d) Cross-sectional SEM image of the GaN/β-Ga_2O_3 interface.

under bias, thereby improving carrier diffusion and migration. Moreover, the high electrode perimeter/area ratio of the interdigital electrode leads to superior carrier collection efficiency and transient speed under zero bias. In this study, we fabricated the interdigitated n-Ga_2O_3 layer by etching Metal-Organic Chemical Vapor Deposition (MOCVD) grown β-Ga_2O_3 thin film and subsequently depositing finger electrodes to enhance carrier collection and built-in electric field strength, rendering a highly efficient β-Ga_2O_3 UVC PD. Fast-transient lifetimes (31 μs 1/e decay and 2.76 μs fast decay component) were obtained by this interdigital structure. The responsivity and UVC selection ratio under self-powered and bias were also enhanced. Additionally, the mechanism of the interdigital structure effect was further investigated. This work will contribute to future research on fast and efficient solar blind detectors.

2. Results and Discussion

Figure 1a shows the X-ray diffraction (XRD) phase analysis of the p-GaN/n-β-Ga_2O_3 thin films. ($\bar{2}$01), ($\bar{4}$02), ($\bar{6}$03) β-Ga_2O_3, and (002), (004) GaN related lattice planes were observed, indicating that the β-Ga_2O_3 grew along the [$\bar{2}$01] single crystal direction. Based on our previous work,[41] the heteroepitaxial β-Ga_2O_3 film exhibited in-plane sixfold twinning polycrystalline due to the crystal matching between hexagonal GaN and monoclinic β-Ga_2O_3. Half width of 2.32° of the XRD rocking curve on the Ga_2O_3 ($\bar{2}$01) plane (Figure 1b) and the non-polarized Raman spectrum (Figure S1, Supporting information) both confirmed the good material quality of our β-Ga_2O_3/GaN epitaxial layers.[42] Figure 1c illustrates the absorbance of β-Ga_2O_3 film grown on double-polished sapphire with identical epitaxial conditions. A bandgap of 4.74 eV was extracted from the Tauc plot of $(\alpha h\nu)^2$ v.s. $h\nu$,[43] which corresponded to 260 nm and was suitable for UVC sensing. Figure 1d displays the cross-sectional scanning electron microscopy (SEM) image of the GaN/Ga_2O_3 interface. An abrupt and clear interface was confirmed with a 510 nm thickness of β-Ga_2O_3. Figure S2, Supporting Information presents an atomic force microscopy (AFM) image of the Ga_2O_3/GaN heterojunction and the stepped structure of GaN/Ga_2O_3 after ion-coupled plasma (ICP) etching, illustrating the smooth Ga_2O_3 (Rq = 1.24 nm) and clear step profile. Hall testing and *C–V* revealed hole concentration of 4×10^{17} cm^{-3} for p-type GaN films and electron concentration of 1.65×10^{16} cm^{-3} for n-type β-Ga_2O_3 films (Figure S3, Supporting Information), which means the depletion region was mainly distributed in the β-Ga_2O_3 layer.

The device fabrication process and detailed information are illustrated in **Figure 2** and **Table 1**. All interdigital-PDs had constant finger length of 1175 μm and device sizes of 1660 μm × 1900 μm. Interdigital-PD groups were constructed with considerations: 1) interdigital-PDs with different mesa finger numbers (period) for investigating electrode perimeter effect (PD_1, PD_2, PD_3, and pad-PD in Table 1); and 2) interdigital-PDs with different duty ratios and electrode spacing while keeping period number constant to study the effect of electric field (column comparison in $PD_{1\text{-}X\ (X = 1\ to\ 3)}$ and $PD_{2\text{-}X\ (X = 1\ to\ 4)}$). Different period numbers induced different electrode perimeters, which was proved to

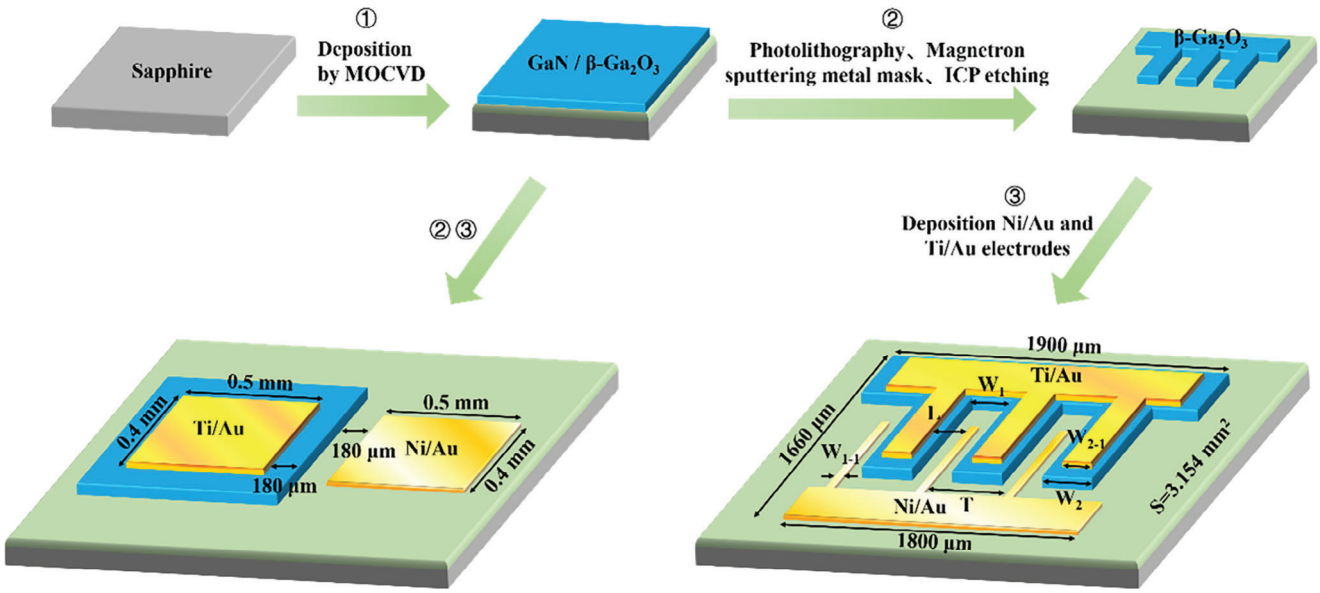

Figure 2. Process flowchart for the p-GaN/n-β-Ga_2O_3 heterojunction photodetector fabrication.

be essential in PD performance at 0 V (shown later), while different duty ratios induced different electric fields at negative bias, which influenced the device performance under bias.

Figure 3a illustrates the linear current-voltage (*I*–*V*) curves of the interdigital-PD with 11 pairs of fingers ($PD_{1\text{-}3}$). It can be observed that this interdigital-PD exhibited distinct rectification characteristics, and the current increased due to the increased carrier concentration by illumination. This effect is particularly prominent under reverse bias after 254 nm illumination because the reverse current at the PN junction is mainly induced by minority carriers. Figure 3b presents the semi-log *I*–*V* curves of interdigital-PD. Under zero bias, the on/off ratio of 254 nm photocurrent to dark current (I_{photo}/I_{dark}) was greater than 10^3, indicating excellent UVC light response characteristics. The photovoltaic effect is the main mechanism of PN-PDs working at 0 V. Figure 3c displays the photovoltaic characteristics of the $PD_{1\text{-}3}$ and pad-PD. In photovoltaic devices, short-circuit current (I_{sc}), open-circuit voltage (V_{oc}) and fill factor (FF) are key parameters. I_{sc} is the current generated and collected without an external power source.[37] V_{oc} is the largest voltage that could be supplied by this PD. FF is the ratio between the $I_{sc} \cdot V_{oc}$ and the largest power. The I_{sc}, V_{oc} and FF of $PD_{1\text{-}3}$ were 1.1 μA, 0.32 V, and 0.38, which were significantly larger than the 14 nA, 0.12 V, and 0.24 of the pad-PD, respectively, indicating higher photovoltaic

Table 1. Summary Table of Parameters for Each PD.

	$PD_{1\text{-}X}$	$PD_{2\text{-}X}$	PD_3	PD-pad
W_1 /$W_{1\text{-}1}$ (μm)	40/20	40/20	40/20	/
W_2 (μm)	100	140	240	/
$W_{2\text{-}1}$ (μm)	50 ($PD_{1\text{-}1}$)	20 ($PD_{2\text{-}1}$)	20	/
	60 ($PD_{1\text{-}2}$)	40 ($PD_{2\text{-}2}$)		
	70 ($PD_{1\text{-}3}$)	70 ($PD_{2\text{-}3}$)		
		100 ($PD_{2\text{-}4}$)		
L (μm)	35 ($PD_{1\text{-}1}$)	70 ($PD_{2\text{-}1}$)	120	360
	30 ($PD_{1\text{-}2}$)	60 ($PD_{2\text{-}2}$)		
	25 ($PD_{1\text{-}3}$)	45 ($PD_{2\text{-}3}$)		
		30 ($PD_{2\text{-}4}$)		
T (μm)	140	180	280	1720
Finger pair numbers	11	9	6	1
Electrode Perimeter (cm)	3.364	2.856	2.1	0.18

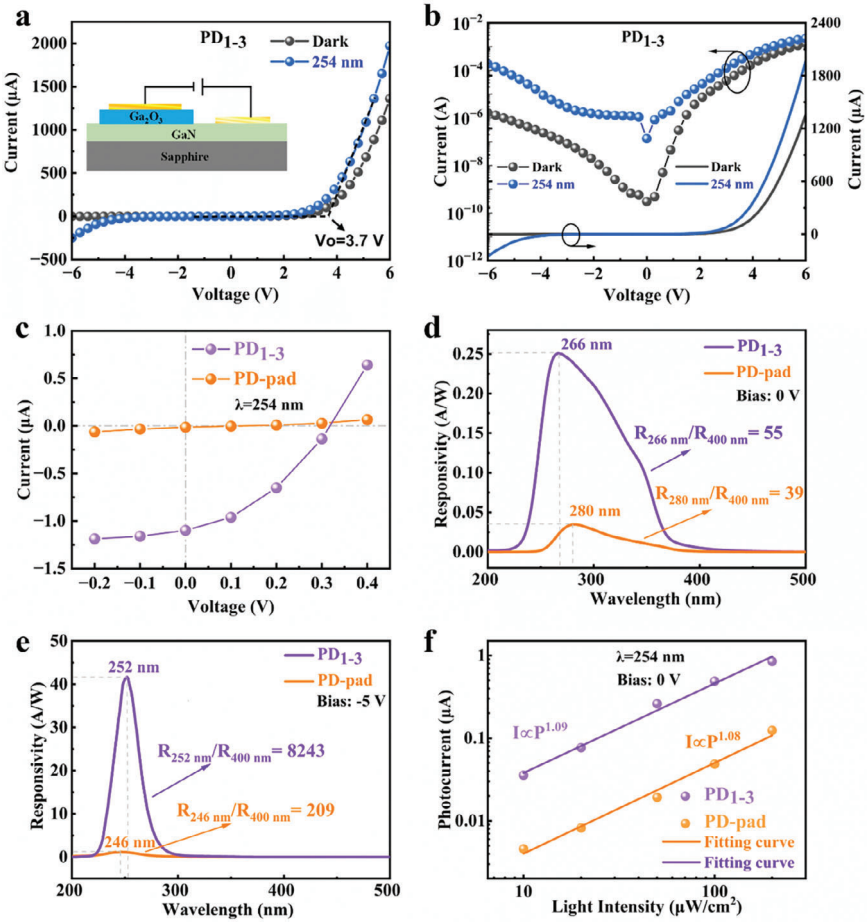

Figure 3. a) Linear *I–V* curves of interdigital-PD (with circuit schematic inset). b) Linear and semi-log plots of *I–V* characteristics of interdigital-PD under 300 μW cm^{-2} 254 nm light sources. c) Photovoltaic characteristics of $PD_{1\text{-}3}$ and pad-PD under 254 nm light. d) Wavelength response curves of both PDs at 0 V bias. e) Wavelength response curves of both PDs at −5 V bias. f) Relationship between photocurrent and light intensity of both PDs at 0 V bias.

conversion efficiency and better self-powered capability of interdigital-PD. Responsivity ($R = \frac{I_p - I_d}{P_\lambda S}$) and detectivity ($D^* = \frac{RS^{1/2}}{(2qI_d)^{1/2}}$) are used to characterize the photoconversion capability of PD, where I_p is the photocurrent, I_d is the dark current, P_λ is the optical power density, q is the elemental charge and S is the effective illuminated area. As shown in Figure 3d, under zero bias, $PD_{1\text{-}3}$ exhibited $R = 0.25$ A W^{-1} @ 264 nm and $D^* = 3.3 \times 10^{12}$ Jones, which were superior to the 35 mA W^{-1} @ 280 nm and 2.16×10^{11} Jones of pad-PD. The higher responsivity of interdigital-PD can be attributed to the longer carrier collection length (electrode's perimeter) of the cross-finger structure under the same device size. The UVC/visible suppression ratio ($R_{266\text{ nm}}/R_{400\text{ nm}}$) for interdigital-PD and pad-PD was 55 and 39, respectively. Interdigital-PD exhibited better spectral selectivity compared to pad-PD. The blueshift of peak wavelength and higher UVC/visible ratio in interdigital-PD compared to pad-PD were ascribed to the smaller exposed area of GaN, which has stronger absorption in UVA and UVB bands.[44] Under a −5 V bias voltage (Figure 3e), the R of $PD_{1\text{-}3}$ was enhanced to 41.71 A W^{-1} @ 254 nm, compared with the 1.2 A W^{-1} @ 246 nm of pad-PD. With applying reverse bias, the built-in electric field in the PN junction increased, leading to a thicker depletion width and more effective separation of photo-generated carriers. Additionally, the barrier height of the Ga_2O_3/metal contact decreased, enhancing the responsivity. It is worth noting that the enhancement effect was significantly higher for interdigital-PD (166 times) than pad-PD (34 times) after applying −5 V bias. This is because the shrunken p/n electrode spacing resulted in a higher electric field in $PD_{1\text{-}3}$, accelerating the drift velocity of carriers and effectively reducing the carriers' scattered probability by defects. The UVC/visible suppression ratio ($R_{266\text{ nm}}/R_{400\text{ nm}}$) of $PD_{1\text{-}3}$ under −5 V was also significantly higher (8243), which was more than 40 times higher than that of pad-PD (209), demonstrating superior spectral selectivity. The enhanced spectral selectivity after reverse bias can be attributed to the widening depletion region. Since the hole concentration of p-GaN was one magnitude larger than the electron concentration of n-Ga_2O_3 (Figure S3, Supporting Information), the depletion region was mainly distributed in the Ga_2O_3 layer. After negative bias was applied, the width of the n-Ga_2O_3 depletion region widened while the p-GaN depletion width was almost not changed, rendering more efficient separation and collection

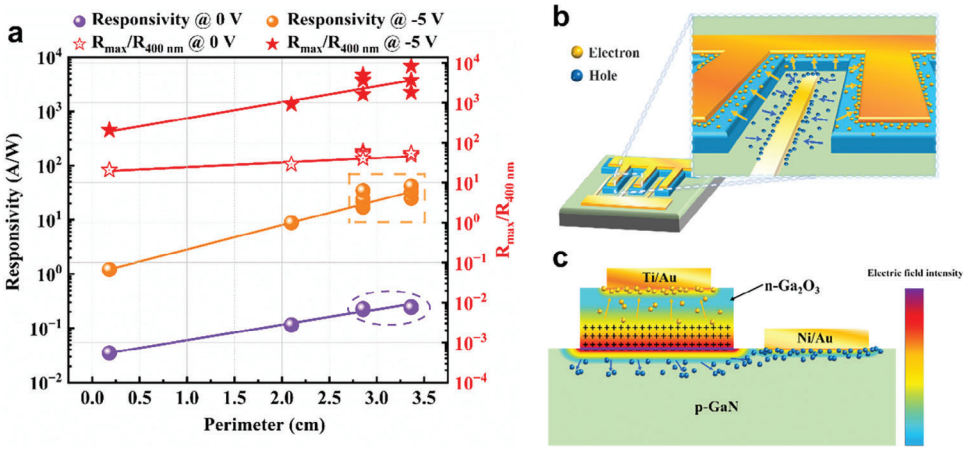

Figure 4. a) Relationship between the perimeter of PDs and their responsivities and spectral selectivity at 0 and −5 V bias voltages. b) The carrier collection diagram of the PD at 0 V. c) The internal carrier transport diagram of the PD under applied bias.

of UVC photo-generated carriers by the n-Ga_2O_3 layer. As for pad-PD, since the built-in electric field was smaller than the one in interdigital-PD, the enhancement effect of the UVC/visible ratio was also weaker. To present a more intuitive UV–visible light suppression ratio, we provided wavelength response curves for the devices in logarithmic coordinates (Figure S4, Supporting Information). Figure 3f shows the relationship between light intensity and photocurrent of $PD_{1\text{-}3}$ and pad-PD. The power-law equation $I_{photo} = AP^{\theta}$ was used to fit the relationship between photocurrent and light intensity, where A is a constant parameter, P is the light intensity, and θ is the exponent of the power law.[45,46] The values of θ for interdigital-PD and pad-PD were 1.09 and 1.08, respectively, with a small deviation from unit, indicating that both PDs had fewer scattering effects from traps and interface defects. This also validated the high quality of our epitaxial crystals and defect passivation in the fabrication process.

To further study the influence of interdigital geometry on PD's performance, multiple interdigital-PDs with different finger numbers and duty ratios were fabricated and compared, as shown in Table 1. We summarized the responsivities of these interdigital-PDs in **Figure 4**a, and found that the perimeter was the key parameter to determine the R at 0 V. At 0 V bias, the R and UVC/visible ratio of the PDs solely increased with electrode perimeter which induced higher carrier collection efficiency. Their detailed $R{\sim}\lambda$ curves are shown in Figure S5, Supporting Information. It is interesting to note that in the purple dash box of Figure 4a, both data points represent 3–4 interdigital-PDs with the same perimeter but different duty ratio ($PD_{1\text{-}X}$ and $PD_{2\text{-}X}$). $PD_{1\text{-}X}$ exhibited responsivity in the range of 0.22 to 0.23 A W^{-1}, and $PD_{2\text{-}X}$ fell within the range of 0.24 to 0.25 A W^{-1}, resulting in an overlapping appearance in Figure 4a. To distinguish these overlapping points with distinct features, we presented an enlarged view of these points in Figure S6, Supporting Information. The R and UVC/visible ratios of these PDs coincided with each other and were solely determined by the electrode perimeter, proving the essence of the electrode perimeter at 0 V. Based on this, a simplified schematic of carrier collection in the PD is depicted in Figure 4b. At 0 V, photo-generated carriers were first dissociated by a vertical built-in electric field, then horizontally diffused toward electrode perimeter and been collected. Therefore, the perimeter was important for self-power status. After applying reverse bias, as shown in the orange box, the R and UVC/visible ratio of PDs with the same perimeter but different duty ratios (thus electrode spacing) diverged. Similarly, in Figure 4c, the internal carrier transport diagram of the PD under applied bias is illustrated. Under bias, the depletion region covered the whole n-Ga_2O_3 layer, and carriers could drift more efficiently toward electrodes by electric field. Therefore, the electric field is also one of the determination factors under bias. With shorter electrode distances (L), the responsivity of PDs increased, as shown in Figure S5d–e, Supporting Information. In conclusion, the interdigital structure in PN-PDs can enhance the carriers' collection at 0 V by having a longer perimeter and elevate the PDs' responsivity under bias by having a larger built-in electric field. To provide a more detailed explanation of the device's operation, we plotted the energy band diagram of the Ga_2O_3/GaN heterojunction in Figure S7, Supporting Information.

Response speed is another important parameter in high-frequency PDs, which determines the optical communication bandwidth. I–T curves of $PD_{1\text{-}3}$ and pad-PD were measured first by light shutter and Keithley 2450 (Figure S8, Supporting Information). Both PDs exhibited swift responses beyond the Keithley 2450 sampling limitation of 20 ms. Therefore, an OPOTEK tunable wavelength pulsed laser and oscilloscope were then adopted to measure the transient decay signal of PDs. The voltage of the series resistor was recorded by an oscilloscope and converted into the I–T characteristics of PDs with a sampling interval of 25 ns, as shown in **Figure 5**a. The transient responses of both PDs under a 260 nm pulse laser are shown in Figure 5b, c. At 0 V bias, both PDs exhibited super-fast 1/e decay (single exponent fitting) time of 31 µs and 76 µs, confirming good crystalline quality, high carrier mobility and optimized device structure. The faster response speed of interdigital-PD can be attributed to the lower series resistance, resulting in a reduced RC time constant. After applying a reverse bias of −10 V, both PDs' decay time increased due to the gradual release of trapped electrons and holes under the applied bias, which was in line with other groups' reports.[34,47] The response speed of interdigital-PD under bias was still faster than pad-PD. This is because the interdigital electrode enhances the electric field in the photosensitive

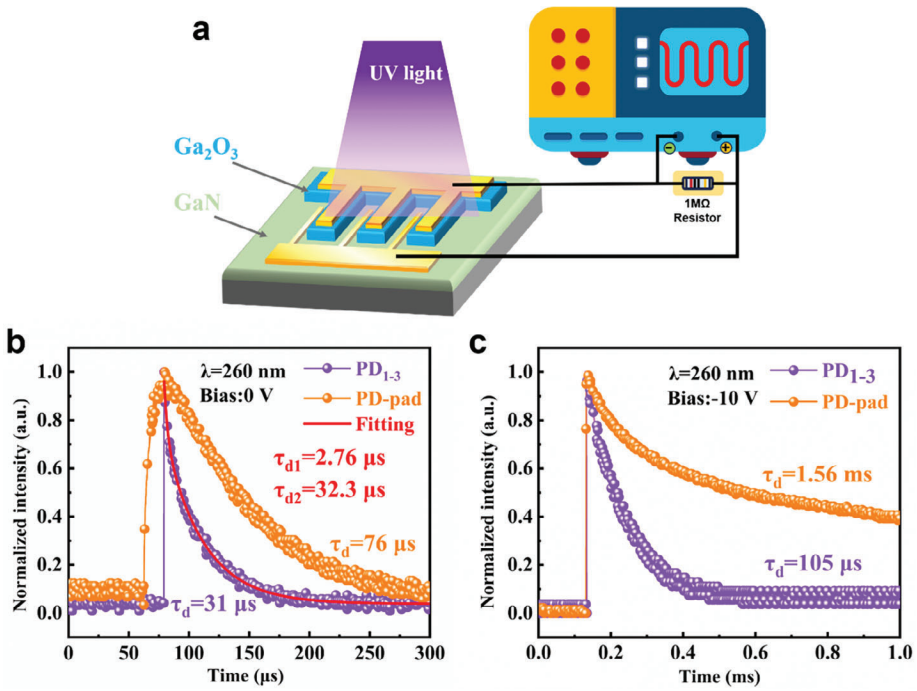

Figure 5. a) Schematic circuit configuration for testing the transient pulse photo response. b) The transient light response curves of interdigital-PD and pad-PD under 260 nm illumination at b) zero bias; c) −10 V bias

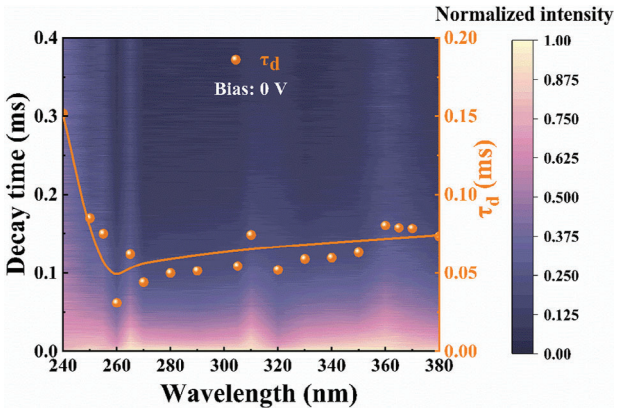

Figure 6. Response decay process of PD_{1-3} under pulsed laser irradiation of 240–380 nm at 0 V (the orange line in the figure corresponds to the 1/e decay time of the PD).

Ga_2O_3 region, leading to an increase in carrier velocity. In some literature, double-exponential fitting was utilized to extract the fast and slow processes. The fast process reflected the variation of carrier concentration after the light was off, which reflects carrier mobility. The slow process was attributed to the capture and release of carriers by defects.[48] In this study, double-exponential fitting was also conducted to analyze the transient response of PD_{1-3} at zero bias, as shown in Figure 5b. The fast and slow decay times were only 2.76 and 31 μs, respectively, which were superior to the-state-of-the-art results.[34,37,49–51]

Figure 6 shows the contour plot of PD_{1-3}'s response decay process under varied excitation wavelengths. The orange line represents the PD_{1-3}'s 1/e decay time. Across the entire 240–380 nm wavelength range, the PD's response speed remained in the order of tens of microseconds, showcasing its exceptionally fast response characteristics. This highlights the outstanding performance of the PD and its suitability for various detection applications. Excited by photons with wavelengths shorter than 260 nm, PD showed a longer decay time (150 μs at 240 nm), which was induced by the carriers' relaxation process from higher conduction band energy levels to the band edge. The PD exhibited the fastest response speed under 260 nm light illumination, corresponding to the coherent excitation of Ga_2O_3 (4.74 eV by absorption spectrum), eliminating the carrier relaxation time.

Table 2 and **Figure 7** summarize and compare performances of Ga_2O_3-based heterojunction PDs. Both the 1/e decay time of 31 μs and fast decay time of 2.76 μs of our devices showed at least 1–2 orders superior to the past reported of Ga_2O_3-based PDs. This ultra-fast response merit can be explained by good material quality and an optimized interdigital structure. The responsivity and response time are located in the left-up corner of Figure 7, showing that our interdigital PDs overcame the trade-off between response time and responsivity in the Ga_2O_3-based UVCPD community. In the future, by employing techniques such as transparent electrodes, optimizing active layer thickness and doping concentration and enhancing crystal quality, it is possible to further improve the device's responsivity.

The response speeds of multiple sets of PDs are compared in Figure S9, Supporting Information. Consistent with the impact of the electrode structure on responsivity, at 0 V bias, the response time of PDs solely decreased with electrode perimeter. The faster transient time with a longer perimeter was due to the smaller resistance, which has been confirmed by the higher photocurrent

Table 2. Comparison of the performances of Ga_2O_3-based self-powered heterojunction ultraviolet photodetectors to date.

Heterojunction	Method of deposition	Responsivity [A W^{-1}]	Decay time [ms]	Ref
Graphene/vertical Ga_2O_3 nanowire	Thermal oxidation of GaN nanowires	1.85×10^{-2} @−5 V	8**	[52]
β-Ga_2O_3/ZnO	PLD	3.5×10^{-1} @−5 V	670/9020 ##	[49]
β-Ga_2O_3/GaN nanowire	CVD	2.75×10^{-2} @−10 V	0.23**	[53]
β-Ga_2O_3/SiC	MBE	1.8×10^{-2} @−10 V	1730/15 220 ##	[51]
Ga_2O_3/Sb_2Se_3 thin film	MBE	9.28×10^{-3} @0 V	0.822**	[54]
ZnO/Ga_2O_3 core–shell microwire	CVD	9.7×10^{-3} @0 V	0.9**	[55]
PEDOTs/Ga_2O_3	CVD	2.6 @0 V	3**	[56]
GaN/Sn: Ga_2O_3 p-n thin film	PLD	3.05 @0 V	18/148 ##	[34]
β-Ga_2O_3/GaN thin films	Gallium evaporative in oxygen plasma	0.18 @0 V	0.3**	[57]
GaN/Ga_2O_3 thin films	PLD	0.0284 @0 V	70**	[58]
n-Ga_2O_3/p-GaN	PLD	0.014 @0 V	0.318/5.9##	[37]
n-Ga_2O_3/i-Ga_2O_3/p-GaN	PLD	0.072 @0 V	0.19/2.4##	[37]
NGr/Ga_2O_3/GaN	Oxidation of gallium	0.0081 @0 V	0.02/3.49##	[50]
n-Ga_2O_3/p-GaN	MOCVD	0.25 @0 V	***0.031*** ** @0 V	***This work***
		41.6 @−5 V	***0.00276***/0.032 ## @0 V	
			0.105 ** @−5 V	

[a] ** Single-exponential decay time; [b] ## Double-exponential decay time.

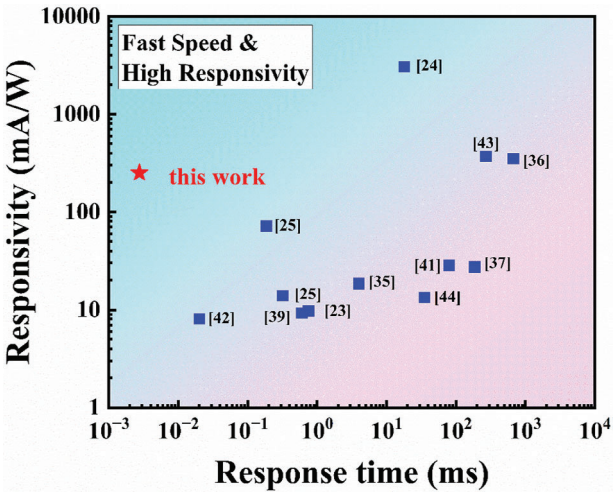

Figure 7. Performance comparison of the responsivity and fast component response time between this study and other reported Ga_2O_3 photodetectors.

at 0 V (Figure S10, Supporting Information). When a reverse bias is applied, the introduction of electric field modulation leads to a faster migration of carriers with smaller electrode spacing. As a result, the perimeter was no longer the sole influencing factor for the response time, and the response time of the photodetector also decreased with the electrode spacing.

3. Conclusion

In conclusion, interdigital structures were applied to p-GaN/n-Ga_2O_3 hetero-junction UVCPDs. Fast transient properties with 2.76 µs fast component and 31 µs 1/e time, high responsivity with 0.25 A W^{-1}@0 V and 41.6 A W^{-1} @−5 V and high UVC selection ratio of 8.2×10^3 were obtained. The longer electrode perimeter and narrow electrode spacing of the interdigital structure not only enhanced the carrier collection efficiency at 0 V, but also increased the built-in electric field at negative bias, rendering a significant improvement in PDs' performance. Under 0 V self-powered mode, electrode perimeter is the sole factor determining static and transient properties, while electrode spacing is another essential factor under negative bias. This work not only presented a super-fast and highly performed solar blind PD, but also investigated the key parameters in designing gallium oxide-based PN-PDs.

4. Experimental Section

A 2 µm [0001]-oriented p-GaN layer and a 2 µm unintended doped GaN layer were first epitaxially grown on c-sapphire by MOCVD. Triethylgallium (TEGa) and oxygen were then used as gallium and oxygen sources to deposit 510 nm n-type β-Ga_2O_3 thin films on a p-GaN template. The growth of β-Ga_2O_3 was performed at 800 °C and 40 Torr. The crystalline quality, carrier concentration and absorption coefficient of these thin films were characterized using XRD, Raman spectrum, SEM, Hall measurement and

UV spectrophotometer, respectively. In the fabrication of the interdigital PN junction photodetector (interdigital-PD), the n-Ga_2O_3 layer was first etched by ICP etcher to form the interdigitated mesa structure. β-Ga_2O_3 mesa structures with various finger pair numbers (6–11 pairs), electrode spacing (25–70 μm) and mesa width (100–240 μm) were designed. Ti/Au (70 nm/100 nm) metal electrodes were then sputtered on the β-Ga_2O_3 finger mesa, followed by rapid annealing at 470 °C in nitrogen for 30 s. Subsequently, Ni/Au (20 nm/100 nm) electrode fingers were deposited on the exposed p-GaN fingers, followed by rapid annealing at 700 °C in nitrogen for 1 min. For comparison, bench-mark PN photodetectors with pad electrode structures (pad-PD) were also fabricated. The ICP etching depth, metal thickness and processes were all identical with those of interdigital-PD, except the mesa design of β-Ga_2O_3 and metal pattern. The PD response properties were measured using the Zolix DSR600 spectrometer and the Keithley 2450. The transient response curve was recorded using OPOTEK wavelength tunable (200–1100 nm) pulsed lasers with 20 Hz, a 6 ns pulse width and an oscilloscope.

Supporting Information

Supporting Information is available from the Wiley Online Library or from the author.

Acknowledgements

This work was supported by National Natural Science Foundation of China (62174140) and Fundamental Research Funds for the Central Universities (20720220077). This research did not receive any specific grants from funding agencies in the public, commercial, or not-for-profit sectors.

Conflict of Interest

The authors declare no conflict of interest.

Author Contributions

Z.C.: Methodology, Investigation, Data Collection, Formal Analysis, Writing – Original Draft, Writing – Review & Editing, Critical Revision of the Article for Important Intellectual Content. X.H.: Methodology, Investigation, Data Collection, Formal Analysis. K.W.: Data Collection, Formal Analysis. X.H.: Investigation. Y.M.: Methodology Visualization. L.Y.: Methodology Visualization. B.Z.: Project administration. H.L.: Conceptualization, Supervision, Review & Editing, Critical Revision of the Article for Important Intellectual Content. All authors contributed to extensive discussions of the results.

Data Availability Statement

The data that support the findings of this study are available from the corresponding author upon reasonable request.

Keywords

Ga_2O_3, interdigital structure, response time, uvc photodetectors

Received: August 30, 2023
Revised: November 1, 2023
Published online:

[1] X. H. Xie, Z. Z. Zhang, B. H. Li, S. P. Wang, M. M. Jiang, C. X. Shan, D. X. Zhao, H. Y. Chen, D. Z. Shen, *Appl. Phys. Lett.* **2013**, *102*, 231122.
[2] H. Lu, W. Tian, F. Cao, Y. Ma, B. Gu, L. Li, *Adv. Funct. Mater.* **2016**, *26*, 1296.
[3] T. Tut, T. Yelboga, E. Ulker, E. Ozbay, *Appl. Phys. Lett.* **2008**, *92*, 103502.
[4] Y. Qin, S. Long, H. Dong, Q. He, G. Jian, Y. Zhang, X. Hou, P. Tan, Z. Zhang, H. Lv, Q. Liu, M. Liu, *Chin. Phys. B* **2019**, *28*, 018501.
[5] Z. Li, T. Yan, X. Fang, *Nat. Rev. Mater.* **2023**, *8*, 587.
[6] H. Chen, H. Liu, Z. Zhang, K. Hu, X. Fang, *Adv. Mater.* **2016**, *28*, 403.
[7] R. Dahal, T. M. Al Tahtamouni, Z. Y. Fan, J. Y. Lin, H. X. Jiang, *Appl. Phys. Lett.* **2007**, *90*, 263505.
[8] E. V. Gorokhov, A. N. Magunov, V. S. Feshchenko, A. A. Altukhov, *Instrum. Exp. Tech.* **2008**, *51*, 280.
[9] L. K. Wang, Z. G. Ju, C. X. Shan, J. Zheng, D. Z. Shen, B. Yao, D. X. Zhao, Z. Z. Zhang, B. H. Li, J. Y. Zhang, *Solid State Commun.* **2009**, *149*, 2021.
[10] K. Arora, N. Goel, M. Kumar, M. Kumar, *ACS Photonics* **2018**, *5*, 2391.
[11] Y. Chen, Y. Lu, M. Liao, Y. Tian, Q. Liu, C. Gao, X. Yang, C. Shan, *Adv. Funct. Mater.* **2019**, *29*, 1906040.
[12] F. Zhou, H. Gong, M. Xiao, Y. Ma, Z. Wang, X. Yu, L. Li, L. Fu, H. H. Tan, Y. Yang, F.-F. Ren, S. Gu, Y. Zheng, H. Lu, R. Zhang, Y. Zhang, J. Ye, *Nat. Commun.* **2023**, *14*, 4459.
[13] R. Mcclintock, A. Yasan, K. Minder, P. Kung, M. Razeghi, *Appl. Phys. Lett.* **2005**, *87*, 241123.
[14] D. J. H. Lambert, M. M. Wong, U. Chowdhury, C. Collins, T. Li, H. K. Kwon, B. S. Shelton, T. G. Zhu, J. C. Campbell, R. D. Dupuis, *Appl. Phys. Lett.* **2000**, *77*, 1900.
[15] Q. Zheng, F. Huang, K. Ding, J. Huang, D. Chen, Z. Zhan, Z. Lin, *Appl. Phys. Lett.* **2011**, *98*, 221112.
[16] D. Wang, W. Wu, S. Fang, Y. Kang, X. Wang, W. Hu, H. Yu, H. Zhang, X. Liu, Y. Luo, J.-H. He, L. Fu, S. Long, S. Liu, H. Sun, *Light Sci. Appl.* **2022**, *11*, 227.
[17] C.-W. Hsu, L.-J. Chou, *Nano Lett.* **2012**, *12*, 4247.
[18] Z. Ji, J. Du, J. Fan, W. Wang, *Opt. Mater.* **2006**, *28*, 415.
[19] W.-Y. Kong, G.-A. Wu, K.-Y. Wang, T.-F. Zhang, Y.-F. Zou, D.-D. Wang, L.-B. Luo, *Adv. Mater.* **2016**, *28*, 10725.
[20] Y.-C. Shen, P.-H. Huang, C.-Y. Tung, C.-Y. Huang, C.-S. Tan, Y.-S. Huang, L.-J. Chen, J.-H. He, R.-H. Horng, *ACS Appl. Electron. Mater.* **2020**, *2*, 590.
[21] F. Roccaforte, M.-H. Weng, C. Bongiorno, F. Giannazzo, F. Iucolano, V. Raineri, *Appl. Phys. A* **2010**, *100*, 197.
[22] S.-H. Tsai, Y.-C. Shen, C.-Y. Huang, R.-H. Horng, *Appl. Surf. Sci.* **2019**, *496*, 143670.
[23] Y. Xu, X. Chen, D. Zhou, F. Ren, J. Zhou, S. Bai, H. Lu, S. Gu, R. Zhang, Y. Zheng, J. Ye, *IEEE Trans. Electron Devices* **2019**, *66*, 2276.
[24] R. Xu, X. Ma, Y. Chen, Y. Mei, L. Ying, B. Zhang, H. Long, *Mater. Sci. Semicond. Process.* **2022**, *144*, 106621.
[25] W. Zhang, W. Wang, J. Zhang, T. Zhang, L. Chen, Y. Zhang, Y. Cao, L. Ji, J. Ye, *ACS Appl. Mater. Interfaces* **2023**, *15*, 10868.
[26] Y. Chen, L. Su, M. Jiang, X. Fang, *J. Mater. Sci. Technol.* **2022**, *105*, 259.
[27] W. Song, J. Chen, Z. Li, X. Fang, *Adv. Mater.* **2021**, *33*, 2101059.
[28] S. Fang, L. Li, W. Wang, W. Chen, D. Wang, Y. Kang, X. Liu, H. Jia, Y. Luo, H. Yu, M. H. Memon, W. Hu, B. S. Ooi, J.-H. He, H. Sun, *Adv. Mater.* **2023**, *35*, 2300911.
[29] D. Wang, X. Liu, Y. Kang, X. Wang, Y. Wu, S. Fang, H. Yu, M. H. Memon, H. Zhang, W. Hu, Z. Mi, L. Fu, H. Sun, S. Long, *Nat. Electron.* **2021**, *4*, 645.
[30] M. Deng, Z. Li, X. Deng, Y. Hu, X. Fang, *J. Mater. Sci. Technol.* **2023**, *164*, 150.
[31] G. Yang, S. Jang, F. Ren, S. J. Pearton, J. Kim, *ACS Appl. Mater. Interfaces* **2017**, *9*, 40471.

[32] M. Ding, W. Hao, S. Yu, Y. Liu, Y. Zou, G. Xu, X. Zhao, X. Hou, S. Long, *IEEE Electron Device Lett.* **2023**, *44*, 277.
[33] Z. Lv, S. Yan, W. Mu, Y. Liu, Q. Xin, Y. Liu, Z. Jia, X. Tao, *Adv. Mater. Interfaces* **2023**, *10*, 2202130.
[34] D. Guo, Y. Su, H. Shi, P. Li, N. Zhao, J. Ye, S. Wang, A. Liu, Z. Chen, C. Li, W. Tang, *ACS Nano* **2018**, *12*, 12827.
[35] S. Li, D. Guo, P. Li, X. Wang, Y. Wang, Z. Yan, Z. Liu, Y. Zhi, Y. Huang, Z. Wu, W. Tang, *ACS Appl. Mater. Interfaces* **2019**, *11*, 35105.
[36] J. Yu, L. Dong, B. Peng, L. Yuan, Y. Huang, L. Zhang, Y. Zhang, R. Jia, *J. Alloys Compd.* **2020**, *821*, 153532.
[37] W. Chen, X. Xu, M. Li, S. Kuang, K. H. L. Zhang, Q. Cheng, *Adv. Opt. Mater.* **2023**, *11*, 2202847.
[38] M. Chen, Z. Zhang, Z. Lv, R. Zhan, H. Chen, H. Jiang, J. Chen, *ACS Appl. Nano Mater.* **2022**, *5*, 351.
[39] Y.-C. Chen, Y.-J. Lu, C.-N. Lin, Y.-Z. Tian, C.-J. Gao, L. Dong, C.-X. Shan, *J. Mater. Chem. C* **2018**, *6*, 5727.
[40] H. Sheoran, S. Fang, F. Liang, Z. Huang, S. Kaushik, N. Manikanthababu, X. Zhao, H. Sun, R. Singh, S. Long, *ACS Appl. Mater. Interfaces* **2022**, *14*, 52096.
[41] X. Ma, R. Xu, Y. Mei, L. Ying, B. Zhang, H. Long, *Semicond. Sci. Technol.* **2022**, *37*, 035003.
[42] Y. Zhu, K. Liu, Q. Ai, Q. Hou, X. Chen, Z. Zhang, X. Xie, B. Li, D. Shen, *J. Mater. Chem. C* **2020**, *8*, 2719.
[43] C. Wu, L. Qiu, S. Li, D. Guo, P. Li, S. Wang, P. Du, Z. Chen, A. Liu, X. Wang, H. Wu, F. Wu, W. Tang, *Mater. Today Phys.* **2021**, *17*, 100335.
[44] P.-F. Chi, F.-W. Lin, M.-L. Lee, J.-K. Sheu, *ACS Photonics* **2022**, *9*, 1002.
[45] Y. Wang, Z. Yang, H. Li, S. Li, Y. Zhi, Z. Yan, X. Huang, X. Wei, W. Tang, Z. Wu, *ACS Appl. Mater. Interfaces* **2020**, *12*, 47714.
[46] H. Mo, X. Zhang, Y. Liu, P. Kang, H. Nan, X. Gu, K. K. Ostrikov, S. Xiao, *ACS Appl. Mater. Interfaces* **2019**, *11*, 39077.
[47] D. Guo, H. Liu, P. Li, Z. Wu, S. Wang, C. Cui, C. Li, W. Tang, *ACS Appl. Mater. Interfaces* **2017**, *9*, 1619.
[48] D. Y. Guo, Z. P. Wu, Y. H. An, X. C. Guo, X. L. Chu, C. L. Sun, L. H. Li, P. G. Li, W. H. Tang, *Appl. Phys. Lett.* **2014**, *105*, 023507.
[49] D. Y. Guo, H. Z. Shi, Y. P. Qian, M. Lv, P. G. Li, Y. L. Su, Q. Liu, K. Chen, S. L. Wang, C. Cui, C. R. Li, W. H. Tang, *Semicond. Sci. Technol.* **2017**, *32*, 03LT01.
[50] Y. Han, Y. Wang, D. Xia, S. Fu, C. Gao, J. Ma, H. Xu, B. Li, A. Shen, Y. Liu, *Small Methods* **2023**, *7*, 2300041.
[51] Y. Qu, Z. Wu, M. Ai, D. Guo, Y. An, H. Yang, L. Li, W. Tang, *J. Alloys Compd.* **2016**, *680*, 247.
[52] T. He, Y. Zhao, X. Zhang, W. Lin, K. Fu, C. Sun, F. Shi, X. Ding, G. Yu, K. Zhang, S. Lu, X. Zhang, B. Zhang, *Nanophotonics* **2018**, *7*, 1557.
[53] W. Ding, X. Meng, *J. Alloys Compd.* **2021**, *866*, 157564.
[54] N. Zhou, *IOP Conf. Ser.: Earth Environ. Sci.* **2020**, *440*, 052031.
[55] B. Zhao, F. Wang, H. Chen, L. Zheng, L. Su, D. Zhao, X. Fang, *Adv. Funct. Mater.* **2017**, *27*, 1700264.
[56] H. Wang, H. Chen, L. Li, Y. Wang, L. Su, W. Bian, B. Li, X. Fang, *J. Phys. Chem. Lett.* **2019**, *10*, 6850.
[57] S. Nakagomi, T.-A. Sato, Y. Takahashi, Y. Kokubun, *Sens. Actuators, A* **2015**, *232*, 208.
[58] R. M. Li, X. Su, S. H. Lim, N. T. K. Thanh, *J. Mater. Chem. C* **2017**, *4*, 53.

